Journal Pre-proof

Fabrication and study of self-assembled NiO surface networks assisted by Sn doping

M. Taeño, D. Maestre, A. Cremades

PII: S0925-8388(20)30535-1

DOI: https://doi.org/10.1016/j.jallcom.2020.154172

Reference: JALCOM 154172

To appear in: *Journal of Alloys and Compounds*

Received Date: 5 December 2019

Revised Date: 29 January 2020

Accepted Date: 3 February 2020

Please cite this article as: M. Taeño, D. Maestre, A. Cremades, Fabrication and study of self-assembled NiO surface networks assisted by Sn doping, *Journal of Alloys and Compounds* (2020), doi: https://doi.org/10.1016/j.jallcom.2020.154172.

This is a PDF file of an article that has undergone enhancements after acceptance, such as the addition of a cover page and metadata, and formatting for readability, but it is not yet the definitive version of record. This version will undergo additional copyediting, typesetting and review before it is published in its final form, but we are providing this version to give early visibility of the article. Please note that, during the production process, errors may be discovered which could affect the content, and all legal disclaimers that apply to the journal pertain.

© 2020 Published by Elsevier B.V.

Journal Pre-proof

Credit Author Statement

The manuscript was written through contributions of all authors. All authors have given approval to the final version of the manuscript. All the author contributed equally.

M. Taeño: conceptualization, methodology, validation, formal analysis, investigation, resources, writing- original draft, writing- review and editing, visualization

D. Maestre: conceptualization, methodology, validation, formal analysis, investigation, resources, writing- original draft, writing- review and editing, visualization, supervision

A. Cremades: conceptualization, methodology, validation, formal analysis, investigation, resources, writing- original draft, writing- review and editing, visualization, supervision, project administration, funding acquisition

Journal Pre-proof

Journal Pre-proof

Fabrication and Study of Self-assembled NiO Surface Networks Assisted by Sn Doping

M. Taeño, D. Maestre and A. Cremades*

Departamento Física de Materiales, Facultad de CC. Físicas, Universidad Complutense de Madrid, 28040, Madrid, Spain

KEYWORDS: NiO, Surface-patterning, luminescence

ABSTRACT

Complex pattering of surfaces commonly requires a significant effort in terms of time, cost, and advanced post-fabrication treatments design, which could be overcome by self-organization mechanisms avoiding damage to the surface materials and enhancing properties of interest. In the present work, grid self-assembled NiO complex surfaces have been fabricated assisted by Sn incorporation during growth, following thermal treatments at 1400 ºC under a controlled Ar flow. The singular morphologies achieved enable the fabrication of robust high surface to volume ratio surfaces with a wide range of surface properties and functionalities. Based on the research performed by a set of complementary techniques, the mechanisms involved in the formation of these textured surfaces have been discussed and some of the fundamental electronic and optical properties of NiO have been analyzed, both aspects necessary to head up the potential

Journal Pre-proof

development of applications based on this p-type material which is arousing growing attention. These singular micro- and nanostructures present high luminescence and tunable performance unusual to bulk NiO samples, which can broaden the applicability of this material to light-emitting devices. Moreover, the surface evolution depends on a controllable way on the preferential state of charge of the incorporated Sn, which could be selected through the convenient Sn-based precursor, its ratio to the metallic Ni starting precursor, and the atmosphere and duration of the fabrication treatment. Finally, in order to assess the dependence of some potential NiO-based applications on the insights achieved on the surface characterization, the gas-sensing response to ethanol from the Sn doped NiO samples was also evaluated. The study of the processes and mechanisms involved in the growth of these grid-patterned surfaces can be extended to similar oxide-based systems.

1. Introduction

NiO is a wide band gap material with good electrochemical stability, high ionization potential, low cost and promising electronic and optical properties which covers a wide range of applications in electrochromic devices, supercapacitors, high-frequency electronics, photocatalyst, solar cells or chemical/gas sensors among others [1,4]. The current increasing interest aroused by nickel oxide is based on the necessity of p-type oxide materials with significant electrical and optical behaviour, the achievement of which requires a deeper understanding of the fundamental properties of NiO as well as an improvement of the synthesis methods. Besides, despite recent developments, p-type oxides, such as NiO, still lag in performance behind the well-known n-type semiconducting oxides, which motivates this study. Non-stoichiometric NiO exhibits a characteristic p-type conductivity due to the inherent Ni

deficiency which is commonly associated with the formation of Ni^{3+} in order to maintain charge neutrality [5]. Doping with different elements can also lead to engineering the NiO stoichiometry by varying the presence of defects, hence modifying the related electrical and optical performance and promoting new functionalities. As some examples, substitutional metal cations with different oxidation states, such as $Nb^{5+,}$ Sn^{4+}, Li^{+}, can lead to tuned concentration of Ni vacancies and Ni^{3+} in NiO, [5,7] which affects the p-type conductivity, and therefore the gas sensing response or the catalytic performance. In particular, Sn doped NiO is commonly reported to exhibit improved conductivity and enhanced gas sensing response, [8,9] however a deeper understanding of the mechanisms behind the NiO response, together with the potential development of Sn doped NiO based devices in emerging fields of research still require to be further explored. Although substitutional Sn^{4+} is commonly considered in Sn doped NiO, the presence of tin with mixed oxidation states should be also considered as it can lead to more complex structure of defects, and variable related chemical, electrical and optical behaviour. Different chemical and physical methods, such as hydrothermal, sol-gel, PLD, spray pyrolysis, CVD or thermal oxidation of Ni, have been employed so far to synthesize NiO in form of nanoparticles, thin films or ceramic materials [1,2,4,10]. However, the necessity of challenging functionalities requires to synthesize and exploit more complex NiO micro and nanostructures, as those described in this work.

In this work we have investigated Sn doped NiO samples synthesized by thermal treatments under the presence of a continuous Ar flow, using metallic Ni and either SnO_2 or metallic Sn as precursors. Self-assembled grid pattern, microwires and complex micro and nanostructures have been achieved at the surface of the treated samples, and analyzed by means of diverse complementary techniques.

Journal Pre-proof

The samples were characterized by means of X-ray diffraction (XRD), scanning electron microscopy (SEM), energy dispersive x-ray spectroscopy (EDS), cathodoluminescence in a SEM, Raman spectroscopy, and X-ray photoelectron spectroscopy (XPS). The gas sensing response to ethanol was also preliminary studied.

2. Material and methods

In this work metallic Ni (Sigma Aldrich 99.99 %) mixed in a controlled ratio with either SnO_2 (Sigma Aldrich 99.9 %) or metallic Sn (Sigma Aldrich 99.8 %) were used as precursor materials for the fabrication of Sn doped NiO micro and nanostructures. The initial powders were mixed in different weight ratios and milled in a centrifugal mill during 5 hours, in order to homogenize the precursor mixture, and subsequently pressed into pellets. Based on preliminary studies, thermal treatments were carried out at 1400 °C under a controlled Ar flow (see detailed explanation and experimental set-up in Fig S1). Following this method, that avoids the use of catalysts or templates, different structures and morphologies have been grown on the surface of the treated pellets. Samples fabricated using only metallic Ni as precursor were also analyzed as a reference. The list of samples investigated in this work is included in Table 1.

X-ray diffraction (XRD) measurements were carried out in a PANalytical X`Pert Powder diffractometer using Cu Kα radiation (λ=1.54158 Å) in Bragg-Brentano configuration. Scanning electron microscopy (SEM) analysis was performed using a Leica 440 Stereoscan and a FEI-Inspect S. For the energy dispersive x-ray spectroscopy (EDS) and compositional study, a Bruker AXS 4010 detector mounted on a Leica 440 SEM was used. Raman spectroscopy analysis was performed at room temperature with a Horiba Jobin-Yvon LabRam Hr800 confocal microscope, using as excitation source a He-Ne laser (λ = 633 nm). Cathodoluminescence (CL)

measurements were carried out at 110 K using a Hitachi S2500 SEM with a Hamamatsu PMA-11 CCD. X-ray photoelectron spectroscopy (XPS) study was performed using a 640 eV photon energy with a resolution of 200 meV and spatial resolution down to 250 nm at the ESCA microscopy beamline at the Elettra synchrotron facility in Trieste (Italy). The gas sensing response under the presence of ethanol was tested in different samples following the experimental set-up schemed in **Fig. S6**.

3. Results and discussion

3.1 Morphological characterization

Thermal treatments performed at 1400 °C during 10 hours using only metallic Ni as precursor led to the growth of large grains, tens of microns width, with a terraced appearance. In some cases, a low amount of ordered square cavities resembling inverted pyramids appear at the surface of the micrograins following orthogonal directions (**Fig. 1(a)**). These square microcavities exhibit lateral dimensions of hundreds of nm or even few microns, as shown in the inset in **Fig. 1(a)**. Similar microcavities have been reported for GaN or In_2O_3 associated with strain relaxation processes and pinholes formation [11,12]. Besides, due to the dynamical Ar atmosphere used during the growth, favourable conditions for vapour-solid growth of wires is achieved and as a result a low amount of microwires is also obtained in this sample, as marked with arrows in **Fig. 1(a)**. Only at the edge of the treated pellets the amount of microwires increases, as shown in **Fig. 1(b)**. These NiO wires exhibit lengths of tens of microns and most of them grow from a triangular terraced base, as shown in the inset in **Fig. 1(b)**.

Significant variations in the morphology of the samples treated at 1400 °C are promoted by adding a low amount of SnO_2 in the precursor mixture, as observed in the images in **Fig. 2**.

Regarding the large micrograins formed at the surface of the treated pellets, the presence of SnO_2 in the precursors leads to a lower amount of ordered microcavities and the formation of textured surfaces with complex geometrical features instead, as shown in **Fig. 2(a)** corresponding to the sample Ni:SnO_2-(9:1). **Fig. 2(b)** shows a detail of the surface of a micrograin from the sample in **Fig. 2(a)**, where stepped and singular geometrical patterns can be observed. These geometrical stepped nanostructures with a bicontinuous dendritic appearance cover large regions of the textured surface of the micrograins surface. In this case, the formation of microwires (**Fig. 2(b))** is also achieved by using SnO_2 in the precursors. **Fig. 2(c)** shows a detailed region of the geometrical terraces with nanoporous surfaces observed in the sample Ni: SnO_2-(9:1), where orthogonal branches grow forming 2D-networks. These dendritic nanostructures usually nucleate at the straight edges of the terraces (inset in **Fig. 2(c)**) and grow laterally following orthogonal directions leading to the formation of porous microislands. This characteristic surface promoted by adding SnO_2 in the precursors exhibits a high surface area-to-volume ratio with potential applicability in catalysis, as well as in high temperature templates and scaffolds. Longer treatments extended during 15 hours, have been carried out at 1400 °C in order to study the evolution of these geometrical islands formed at the surface of the micrograins. In this case, an increase in the thickness of the branches forming the characteristic latticework-like structures is promoted, as compared with treatments performed during 10 hours. **Fig. 2(d)** shows the surface of the sample Ni:SnO_2-(9:1)-b where the number of regions with a grid-micropatterning is increased and a 3D-network is initiated. The lateral branches of these geometrical nanostructures reach thickness of tens of nanometres and a vertical growth instead of a laterally one is initiated in this case. The formation of the characteristic grid-patterning and porous microislands promoted by using SnO_2 in the precursors is inhibited when no Ar flow is used during the

Journal Pre-proof

thermal treatment. Besides, in order to study the influence of the concentration of SnO_2 in the precursors, diverse samples have been fabricated following the same thermal treatment but with a higher amount of SnO_2 in the initial mixture. **Fig. 3(a)** shows that the number of geometrical patterns at the surface of the treated pellets is drastically decreased for the sample Ni:SnO_2-(1:1) and the surface of the micrograins exhibit a smoother appearance.

By using a larger amount of SnO_2 in the precursors, Ni:SnO_2-(1:3), the formation of wires and geometrical patterns is inhibited. In that case agglomerated micrograins with lower dimensions are formed at the surface of the treated pellet as compared with the sample Ni:SnO_2-(9:1) and either Sn or Ni-rich regions can be observed as shown in supplementary **Fig. S3(a)**. Finally, a low amount of metallic Sn, instead of SnO_2, has been used in the initial mixture in order to explore the influence of the Sn-based precursor in the growth process. Contrary to the sample Ni:SnO_2-(9:1), when using metallic Sn as precursor the characteristic grid-pattern surface decreased and large micrograins with terraced structures appear instead (**Fig. 3(b)**). Regions with microwires are also formed for this sample, as observed in the top-left region in **Fig. 3(b)**.

Therefore, careful precursor selection allows for tuning the formation of the microwires as well as determining the appearance of complex surface nanostructuring. Only for the samples Ni:SnO_2-(9:1) and Ni:SnO_2-(9:1)-b, textured surfaces and 2D or 3D networks, have been observed. By using metallic Sn as precursor, textured surfaces are inhibited, showing large micrograins with terraced appearance and higher concentration of elongated structures.

3.2 Structural and compositional analysis

Fig. 4 shows the XRD patterns corresponding to the samples fabricated with variable amounts of SnO_2 or Sn in the precursor mixture. XRD pattern from the NiO reference sample is also

included. All the peaks in **Fig. 4** can be assigned to NiO with rock-salt cubic structure, while peaks from the precursors (metallic Ni, Sn or SnO_2), other oxides, or ternary compounds are not observed, even for the sample Ni:SnO_2-(1:1). The addition of a low amount of SnO_2 in the precursor (Ni:SnO_2-(9:1)) induces a slight increase in the relative intensity of the (200) peak, as compared to the reference NiO. However, as the amount of SnO_2 is increased in the precursors the NiO (311) peak exhibits higher relative intensity, as observed for the sample Ni:SnO_2-(1:1). Extended treatments involve an increase in the relative intensity of the (220) peak, as noticed for the sample Ni:SnO_2(9:1)-b (supplementary **Fig. S4(a)**), which could be related to the initiation of the vertical growth and 3D-grid microstructures. On the other hand, when using metallic Sn as precursor, the (220) peak dominates the XRD pattern instead of the (200) one. Moreover, an increase in the relative intensity of the (111) and (311) peaks is also promoted for the sample Ni:Sn-(9:1). Hence, a variable composition in the precursor mixture leads to changes in the XRD signal involving texturing effects in the treated samples. Sn doping and the formation of related defects can alter the surface energy and the growth kinetics of the different planes. A. A. Dahkel [13] reported that by decreasing the concentration of point defects, and hence increasing NiO stoichiometry, a change from (111) to (200) is promoted, which in our case should involve higher defect density for the sample Ni:Sn-(9:1). Moreover, the presence of SnO_2 or Sn in the precursors also promotes a shift to higher diffraction angles, as compared with the reference NiO, (**Fig. 4(b)**), which can be associated with the Sn doping process. This shift, around 0.5°, is more noticeable as the SnO_2 ratio raises and by using Sn as precursor, as observed in **Fig. 4(b)**. As the ionic radii from Sn^{4+} and Ni^{2+} are comparable, 0.71 Å and 0.69 Å respectively, this shift cannot be directly related to lattice contraction owing to substitutional Sn^{4+}.

Actually, different works on Sn doped NiO reported either lattice contraction or expansion owing to substitutional Sn^{4+}, [10,14] hence other factors such as incorporation of tin with variable oxidation states or variation in the concentration of nickel or oxygen vacancies due to charge balance should be considered. Incorporation of Sn^{4+} in Ni^{2+} sites can be compensated either by generation of two electrons (electronic compensation) or by formation of Ni vacancies (ionic compensation) [7]. In our case, a higher presence of cationic vacancies could explain the weak lattice contraction observed by XRD. Moreover, a higher concentration of Ni^{3+} promoted by substitutional Sn^{4+} can also induce lattice shrink as the ionic radius of Ni^{3+} (0.56 Å) is smaller than that from Ni^{2+}. Only for the sample Ni:SnO_2-(1:3) with a higher amount of SnO_2 in the precursors, weak peaks from SnO_2 start to appear in the XRD patterns (see supplementary **Fig. S3(b)**). The intensity of these peaks is very low, despite the high amount of SnO_2 used in the precursors. Hence the initial SnO_2 used in the initial mixture should be either partially evaporated during thermal treatments at 1400 °C or segregated to the inner region of the pellets.

From now on, the analysis of the samples will be focused on the regions of the surface without NiO microwires, the study of which will be completed elsewhere.

Compositional analysis by means of EDS confirms the presence of Ni and O at the surface of the samples fabricated using a low amount of SnO_2 or Sn in the precursors (Ni:SnO_2-(9:1), Ni:Sn-(9:1)) in concentrations different than the theoretical 50 at.%. According to the quantification of the corresponding EDS spectra, after appropriate Bremsstrahlung and ZAF corrections, the amount of Ni is usually higher than O, with a variable Ni/O ratio around 1.5, which could involve NiO_{1-x} sub-stoichiometry or the presence of small Ni clusters. On average, tin is not detected by EDS at the surface of the samples Ni:SnO_2-(9:1) and Ni:Sn-(9:1), considering the detection limit of the technique. It is only when increasing the initial amount of tin oxide, Ni:

SnO_2-(1:3), that Sn-rich regions can be locally detected in the non-homogeneous surface of the treated pellet (supplementary **Fig. S3(a)**). A cross-sectional EDS compositional image from the sample Ni:SnO_2-(9:1)-b, for which a characteristic grid-patterning was observed at the surface, shows that the amount of Sn increases in the inner region of the pellet, while the surface is mainly formed by Ni and O (supplementary **Fig. S4(b)**). This result indicates the presence of a Ni-rich surface and an inner Sn-rich region, probably due to variable cationic diffusivity during crystal growth and possible SnO_2 segregation to the innermost region, as also reported for oxidation of similar Ni-based alloys [15,16].

In summary, XRD patterns from samples with a weight ratio Ni/Sn or SnO_2 9:1, can be indexed with NiO rock-salt structure, not showing peaks related to the presence of Sn based oxides. XRD and EDS analysis indicates a possible SnO_2 segregation to innermost region.

3.3 XPS characterization

In order to achieve a deeper understanding in the formation of the characteristic surface-geometrical features when adding SnO_2 or Sn in the precursors, surface sensitive XPS measurements with spatial resolution have been performed for the samples Ni:SnO_2-(9:1) and Ni:Sn-(9:1), as well as in the reference NiO sample, as shown in **Fig. 5**. One of the main advantages of this technique is the possibility to perform detailed analysis on different points in order to understand Sn incorporation at the surface. The XPS spectra were calibrated using the C-1s signal from adventitious carbon and deconvolutions were carried out using Voigt functions after appropriate Shirley background correction. Ni-3p, O-1s and Sn-3d core levels have been analysed in this case, as well as the valence band region. **Fig. 5(a)** and **5(b)** show XPS images acquired with the Ni-3p signal from diverse regions corresponding to the Ni: SnO_2-(9:1) and

Ni:Sn-(9:1) samples, respectively. XPS spectra from two representative points at each sample, marked in **Fig. 5(a)** and **5(b)**, are shown in **Fig. 5(c)-5(f)**. Points A and A' are related to regions with grid-patterning or wrinkled regions, while points B and B' correspond to smoother surface regions from both samples. **Fig. 5(c)** shows the XPS spectra from Ni-3p core levels, where four main bands can be observed. The low energy bands at 68.6 eV and 70.1 eV are related to Ni $3p_{3/2}$ and Ni $3p_{1/2}$ respectively, due to Ni^{2+} in NiO, whereas the high energy bands at 72.0 and 74.9 eV correspond to the doublet Ni $3p_{3/2}$ and Ni $3p_{1/2}$ from Ni^{3+} [17,18]. These results confirm the presence of Ni^{3+} at the surface of the probed samples, which usually involves formation of Ni vacancies. The Ni^{3+}/Ni^{2+} ratio, estimated from the XPS spectra, indicates values around 0.34 for the reference NiO. This Ni^{3+}/Ni^{2+} ratio ranges from 0.24 (point A) to 0.39 (point B) for the Ni:SnO_2-(9:1) sample, showing a lower value at the point A with cavities and grid-pattering, while values from 0.14 (point A') to 0.19 (point B') are found at the surface of the sample Ni:Sn-(9:1). These results confirm, on average, lower concentration of Ni^{3+} at the surface of the sample fabricated using Sn-based precursors, mainly for the Ni:Sn-(9:1), as compared with the reference NiO, which probably involves higher concentration of Ni vacancies in the latter.

Fig. 5(d) shows the $Sn3d_{3/2}$ and $Sn3d_{5/2}$ core levels obtained from the samples Ni: SnO_2-(9:1) and Ni:Sn-(9:1). In both cases the presence of Sn has been confirmed in different points of the probed surfaces. Two contributions at around 485.7 and 487.4 eV can be observed for the $Sn3d_{5/2}$ signal, which can be assigned Sn^{2+} and Sn^{4+}, respectively [19]. Moreover, incorporation of Sn with variable chemical environment as a function of the probed region should be considered. On average, when using metallic Sn as precursor the presence of Sn^{2+} related contribution is more favorable (both in points A' and B'), while formation of Sn^{4+} is enhanced when using SnO_2 as precursor. In the latter, only the regions with a higher presence of cavities

and grid-patterning (point A in **Fig. 5(a)**) exhibit higher Sn^{2+}/Sn^{4+} ratio. From the analysis of the corresponding XPS spectra, a variable concentration of Sn, with Sn/Ni ratios between 0.2 and 3.6 , has been estimated at the surface of the samples grown using Sn-based precursor, with larger heterogeneity in the concentration of Sn for the sample Ni:Sn-(9:1). As the presence of Sn was hardly detected by EDS in these samples, surface-sensitive XPS results indicate a higher Sn diffusion towards the top-surface of the samples, as compared with the bulk region. XPS measurements also confirm Sn doping and a non-homogeneous incorporation of Sn with variable oxidation states at the surface of the both samples, which should assist the formation of the observed complex surfaces. Therefore, by using different Sn-based precursors either higher or lower Sn^{2+}/Sn^{4+} ratio can be induced at the surface, hence promoting preferential oxidation and tailoring the formation of self-assembled complex networks at the surface.

Fig. 5(e) shows XPS spectra from O 1s core levels. In this case, the spectrum from the reference NiO is dominated by a band centered at around 531.8 eV, which corresponds to lattice O^{2-} in NiO [5]. For the Ni: SnO_2-(9:1) sample, two contributions at low (531.5 eV) and high (533.2 eV) binding energy are observed, being the latter more intense at point A. In the case of Ni:Sn-(9:1) sample, also two contributions are observed, centered around 532.1 eV and 533.8 eV, although in this case the relative intensity of the high energy contribution is higher, mainly at point A', as compared with the other analysed samples. The low energy contribution can be related to lattice O^{2-} in NiO and Ni-O-Sn bonds, while the high energy band is commonly associated with adsorbed oxygen species and hydroxyl groups [5] the concentration of which is promoted by Sn incorporation, and even dominating for the Ni:Sn-(9:1) sample and at regions with higher presence of Sn^{2+}.

It is commonly reported [5-7] that dopants such as Li^{+}, Al^{3+}, Cr^{3+}, Sn^{4+}, or W^{5+} replace Ni^{2+} cations in NiO instead of refilling Ni vacancies [5] hence Ni substitution by Sn has been considered in this work. According to XPS measurements (**Fig. 5(d)**), Sn incorporates mainly as Sn^{2+} for the Ni:Sn-(9:1) sample, while mixed valence states, Sn^{2+} and Sn^{4+}, are found at the surface of the Ni:SnO_2-(9:1) sample. The presence of Sn^{2+} and/or Sn^{4+} also alter the Ni^{3+}/Ni^{2+} ratio at the surface. In this case, the higher presence of Sn^{4+} could lead to enhanced Ni vacancies due to the substitution of Ni^{2+} by Sn^{4+} in order to achieve charge neutrality, as observed for Ni:SnO_2-(9:1). Actually, the presence of Ni^{3+} is lower for the samples in which a higher presence of Sn^{2+} is detected, Ni:Sn-(9:1), which also shows a larger presence of adsorbed oxygen and hydroxyl groups at the surface. These variable surface electronic properties reached as a function of the Sn-based precursor should be considered in order to exploit potential catalysis and gas sensing applications.

The valence band region of the reference NiO, the Ni:SnO_2-(9:1) and Ni:Sn-(9:1) samples have been also investigated. Differences can be appreciated as a function of the employed Sn-based precursor, mainly at the low energy region, as shown in **Fig. 5(f)**. Two main contributions are observed in the valence band region at ~ 2 eV and ~ 4 eV, which are attributed to Ni 3d and O 2p states, respectively [20]. The low energy contribution is enhanced and slightly shifted to higher energy at both points A' and B' from the sample Ni:Sn-(9:1), while for the sample Ni:SnO_2-(9:1) this shoulder is more pronounced in point A with grid-micropatterning and lower Sn^{4+}/Sn^{2+} ratio. Hence an increased amount of Sn^{2+}, as well as lower Ni^{3+}/Ni^{2+} ratio, should be related to the enhancement in the relative intensity of this low energy contribution in the VB region. In our case, the higher relative intensity of the low energy shoulder could be enhanced due to local SnO-like chemical environment associated with the higher presence of Sn^{2+}, as some authors

[21] reported a possible origin of a band at 2.8 eV due to SnO. The energy difference between the Fermi level and the maximum of the valence band ($E_F - E_{VBM}$) has been also estimated for these samples. An averaged value around 1.6 eV has been measured for the reference NiO, while values of 0.8 eV (point A) and 1.6 eV (point B), for the sample Ni:SnO_2-(9:1), and 1.4 eV (point A') and 1.3 eV (point B') for the sample Ni:Sn-(9:1) have been also estimated. These results involve a higher p-type character for the surfaces of the Sn doped samples, mainly for the regions with higher concentration of Sn^{2+}.

The presence of a continuous Ar flow during the thermal treatments, as well as the Sn doping, allow to achieve novel micro- and nanostructures not reported so far for NiO, the study of which can shed light to the growth mechanisms in NiO-based systems and spread the applicability of this p-type semiconductor oxide. The absence of Ar flow, inhibits the growth of textured surface (as well as elongated structures), leading to the formation of surfaces with smooth appearance, as shown in **Fig. S2**. Surface-diffusion mediated processes should be involved in the formation of the characteristic features at the surface of the NiO treated pellets observed in this work. Actually, surface texturing and microstructure evolution related to oxidation processes are usually explained attending to classical crystal growth theories. In this case, oxidation kinetics and diffusion-controlled mechanisms, based on the Wagner´s theory [22] should be considered in the formation of the characteristic grid-micropatterning observed at the surface of the samples analyzed in this work. The presence of a continuous Argon flow employed during the thermal treatments can lead to low oxygen pressure and enhanced supersaturation conditions, which are key factors for the formation of the characteristic surface patterns. In addition, the presence of Sn at the surface should also play a key role in the development of the surface texturing in NiO, leading to preferential diffusion paths, promoting variable oxide formation by lowering

Journal Pre-proof

activation barriers and altering the growth kinetics by enhanced nucleation sites at the surface. Contrary to other reported works [7,8] in this case Sn with mixed oxidation states can be found at the surface of the Sn doped NiO samples. It is commonly accepted that substitutional Sn^{4+} can promote an increase in the concentration of Ni vacancies, thereby favouring Ni diffusion paths and increasing the oxidation rate at the surface. On the other hand, when Ni^{2+} is replaced by isovalent Sn^{2+} the amount of Ni vacancies should not be altered. Therefore, despite the fact that the formation of the characteristic grid-micropatterning is promoted by the presence of Sn^{2+} at the surface, this is not enough and a low amount of Sn^{4+} non-homogeneously distributed at the surface is also required. Hence, formation of the self-assembled NiO surface networks is assisted by selective Sn^{2+} and Sn^{4+} doping.

Moreover, diverse factors, such as presence of impurities, as well as point and extended defects, should be also considered in this case as they can alter the diffusivity of the ionic species and the oxidation rate, which are some of the main parameters governing surface texturing formation. As some examples, Y. Unutulmazsoy et al [16] reported an enhanced oxidation rate in Al doped NiO based on the improved cationic diffusion. W. H. Blades et al [23] reported that an inhomogeneous concentration of Cr can alter Ni oxidation, leading to confinement of Ni atoms to single NiO terraces where new oxide nucleates forming NiO staked islands. Similar effects could be involved in our work, for which non-homogeneous Sn incorporation with different oxidation states has been detected at the surface of the Ni:SnO_2-(9:1) and Ni:Sn-(9:1) samples.

The presence of a NiO-rich surface and an inner region with higher concentration of Sn and/or SnO_2 observed in the treated pellets, confirmed by XRD and EDS, can be explained considering differences in the oxygen affinity and the cationic diffusion coefficients. For NiO, oxygen diffusion coefficient is much lower than Ni diffusion coefficient [24] hence the latter is only

considered at high temperatures as those used in this work for which nickel outward diffusion occurs. Besides, at 1400 °C bulk Ni diffusion governs the growth process instead of grain boundary diffusion [15,25]. In addition, reactivity of Ni and Sn are similar, but the stability of the corresponding oxides and their growth rates are different. As Ni diffusion in NiO is faster than Sn in SnO_2, lateral growth of NiO is promoted at the surface during oxidation. In that case, the faster growth of NiO could overgrow the SnO_2 which remains slow growing, hence developing an outermost NiO region at the surface of the pellets, whereas SnO_2 will remain mainly in the inner region, as observed in this work [26]. Segregation of secondary oxides to the inner region has been also reported for Ni-Cr and Ni-Al alloys during Ni oxidation, in agreement with our results [15,16].

Finally, dendritic and nanoporous surfaces, [27] similar to those observed at the surface of the sample Ni: SnO_2-(9:1), have been commonly reported for dewetting processes which involve self-organization and bicontinuous nanoporous growth if the alloy components are in the appropriate conditions. The solid state dewetting process itself proceeds from the spontaneous formation of voids and holes at specific defects and via flux of material [28] while holes, edges, impurities and grain boundaries are key elements to initialize this process for which the overall driving force is the minimization of surface energy. Similar concepts could be extended to some of the samples under study. Fabrication of complex surface patterning by auto-organization processes, as those described in this work, could ease and optimize the synthesis process while enabling novel functionalities.

3.4 Raman Spectroscopy analysis

Journal Pre-proof

Journal Pre-proof

In order to complete the structural characterization of the samples under study, Raman spectroscopy measurements was also carried out. The bands observed in the normalized Raman spectra shown in **Fig. 6** correspond only to the Raman modes commonly reported for NiO, [29,30]. Raman bands from the precursors or other Ni, or Sn based compounds are not observed in this case, in agreement with XRD results. Raman contributions in **Fig. 6** at 400-450 and 550 cm^{-1} are related to TO and LO modes, respectively. Two-phonon modes are centered at 715 cm^{-1} (2TO) and 1090 cm^{-1} (2LO), and a combination of TO+LO appears at 895 cm^{-1}. The mode at 1490 cm^{-1} corresponds to the two-magnon (2M) excitation. The interpretation of the NiO Raman spectra is not straightforward, as magnetic order can affect phonon energies via spin-phonon coupling. In this case, the Sn-based precursor used in the initial mixture modifies the relative intensity of the Raman modes in the Sn doped samples, as compared with the reference NiO grown from metallic Ni. Actually, samples fabricated with SnO_2 in the precursors exhibit an increase in the relative intensity of the 2M contribution at 1490 cm^{-1}, whereas by using metallic Sn an increase in the relative intensity of the one-phonon modes, especially the LO, is clearly observed. The I_{2M}/I_{LO} ratio changes from 5.84 to 0.34 in the samples Ni:SnO_2(9:1) and Ni:Sn(9:1) respectively, while a value of 1.25 is obtained for reference NiO. Some authors reported that the decrease of the 2M mode is associated with a crystal reconstruction lowering the antiferromagnetic spin correlation and/or defective regions involving decrease in the Ni^{2+} local symmetry [31] which in our work could be enhanced when using metallic Sn in the precursors. Moreover, an increase in the relative intensity of the first order modes has been also attributed to the presence of parity-breaking defects such as nickel vacancies [29,30,32]. Actually X. Xu et al. [5] associate the TO mode with vibrational Ni^{3+}-O modes, while LO mode can be related to Ni^{2+}-O stretching [33]. A blue shift of this LO mode, centered at around 550

cm^{-1}, is also observed in the Sn doped samples fabricated using SnO_2 or Sn, with respect to the reference NiO, which could support the lattice contraction observed by XRD measurements (**Fig. 4**) and the substitution of Ni^{2+} by high oxidation state ions [9]. Besides, changes are also observed in the region around 700 cm^{-1} corresponding to the 2TO mode. Different Raman modes with variable relative intensity can be observed in this complex region. For the NiO reference sample a peak at 745 cm^{-1} can be clearly distinguished, while for the sample Ni:Sn-(9:1) a sharp peak at 710 cm^{-1} and a weak contribution at 684 cm^{-1} are observed. For the samples grown using SnO_2, a broad peak from 680 to 710 cm^{-1} can be appreciated. The origin of these peaks is unknown, although a relation with the presence of the precursor materials or overtone modes have been ruled out in this case. Variations in the spin-phonon coupling and mode-splitting due to the presence of Sn in NiO could be involved in the understanding of this complex region, actually a TO' mode generated by splitting of the TO mode [34] can be observed for the sample Ni:SnO_2(1:1). Moreover, overcome of the selection rules for the Raman modes and activation of possible silent modes in high defective regions should be also considered.

3.5 Optical properties

Only a few works report on the photoluminescence from NiO, but less has been done so far in the cathodoluminescence study of NiO, the analysis of which can shed light to the understanding of the origin of the luminescent properties of NiO. Cathodoluminescence measurements indicate that NiO emission extends from the near-IR to the ultraviolet range and varies as a function of the probed sample, as shown in the normalized CL spectra in **Fig. 7**. CL spectrum from the reference NiO sample exhibits a dominant band at 1.46 eV and emissions with lower relative intensity in the visible (2-2.5 eV) and the ultraviolet range (3.5 eV and 4.5 eV). By adding a low amount of SnO_2 in the precursors, the intensity of the visible emission is drastically increased in

a factor x40. In this case, the CL spectrum from the Sn doped sample Ni: SnO_2-(9:1) is dominated by an intense and narrow orange emission at ~ 2 eV.

When metallic Sn is added in the precursor mixture (Ni:Sn-(9:1)), the visible CL signal is also increased as compared to the reference NiO sample although in a factor x40, and the CL spectrum shows a dominant emission at ~ 2 eV, slightly shifted to lower energy as compared with the CL spectrum form Ni:SnO_2-(9:1). In this case, also a weak shoulder at ~1.5 eV and an emission at 3.27 eV can be observed. If a higher amount of SnO_2 is added in the precursors (Ni: SnO_2-(1:1)), the corresponding CL spectrum shows a wider and more complex visible emission centered at around 2.3 eV and an intense UV emission at around 4.5 eV. XRD measurements confirmed that all these samples consist only of NiO, the wide band gap of which (3.6 – 5 eV) allows UV near band gap emissions and/or excitonic recombinations, and visible or near-IR emissions due to deep levels mainly associated with structural defects. In our work, the use of Sn-based compounds in the precursors induces a remarkable increase of the total NiO luminescence, mainly for the sample Ni:SnO_2-(9:1), in agreement with L. S. Nair et al. [10] which reported an increase in the photoluminescence signal by Sn doping. The origin of the NiO near-infrared band (1.46 eV), which dominates de CL signal for the reference NiO sample, has been associated with transitions between 3d energy levels in impurity or defect-perturbed Ni^{2+} states [35]. Surface reorganization observed for Sn doped NiO samples could decrease the concentration of defects associated with this near-IR emission, or promote different recombination paths. Diverse origins are reported for the complex emissions at the visible range, mainly associated with Ni vacancies defects, Ni^{2+} intrasites, oxygen vacancies and/or interstitial and transitions involving $3d^8$ electrons in Ni^{2+} [32,36]. Z. Zhang et al. [37] reported an emission at 1.84 eV in NiO films associated with oxygen vacancies in NiO, however A. C. Gandhi et al.

[32] studied diverse photoluminescence emissions in the visible range which origins are due to oxygen interstitials (2.05 eV), and recombination of photogenerated holes trapped in deep levels associated with oxygen vacancies and electrons trapped at shallow levels below the conduction band (2.37 eV). In our work, the visible emission observed for the Sn doped NiO samples should be related to native defects in NiO promoted by Sn doping, as this emission is also observed with a lower intensity for the reference NiO sample. Moreover, possible competitive radiative paths could be involved in the near-IR and the visible emissions, as the increase in the relative intensity of the latter involves a decrease in the former. The sample Ni: SnO_2-(9:1), which exhibits a characteristic grid-micropatterning at the surface and Sn doping, is the one with the highest luminescent intensity probably due to presence of cationic and anionic vacancies. Actually, the concentration of Ni vacancies can be increased by Sn doping, thereby enhancing the orange band. Doubly ionized Ni vacancies (V_{Ni}'') are the most commonly reported defects for NiO [16] as formation of single ionized Ni vacancy is only favoured at low temperature and high oxygen pressure, different to the experimental conditions used in the present work. The higher intensity of this orange emission from the Ni:SnO_2-(9:1) sample could be also associated with the presence of mixed Sn^{4+} and Sn^{2+} states at its surface, as compared with the Ni:Sn-(9:1) sample, which probably involves higher Ni deficiency. SnO_2 exhibits a similar orange emission at 1.94 eV associated with oxygen vacancies [38] however in our work no peaks from SnO_2 were observed by XRD or Raman spectroscopy. Different authors associated the emission around 3.2 eV to excitonic recombination and self-trapped d-d charge transfer excitons in NiO [32,36]. The emission at 4.5 eV observed in this work has not been usually reported for NiO, as most works consider a NiO bandgap around 3.6 eV or even lower. W. C. Mackrod et al. [39] considered intraionic d-d transition and/or excitonic recombination in this region. Hence, according to the

CL results analyzed in this work, the NiO luminescent signal can be tailored from the near-IR (1.46 eV) to the UV (4.5 eV) by appropriate Sn doping. Moreover, a low amount of SnO_2 in the precursor mixture induces an intense orange emission, probably related to Ni vacancies formed to compensate charge imbalance, which could extend the applicability of NiO to luminescent and optoelectronic devices, fields in which the use of NiO is still under exploration. By selecting appropriate Sn- based precursor, CL signal can be modulated from near-IR to UV. **Fig. S5**, shows the chromaticity diagram obtained from the measured CL spectra. These results may extend the applicability of these materials to fields in which their use is not exploited, towards the achievement of high intense white luminescence.

3.6. Gas-Sensing Properties

Finally, the gas sensing properties of undoped and Sn doped NiO samples were tested, as a proof to evaluate their potential applicability and assess the dependence of the sensing behaviour on the achievements acquired during the samples characterization. The experimental set-up using for the gas sensing test is schemed in **Fig. S6**. The response to ethanol gas of both the reference NiO sample and the sample Ni:SnO_2-(9:1), for which surface Sn doping was confirmed by XPS, were evaluated at room temperature. Fig. 8 shows the changes in the resistance and subsequent recovery under ethanol or air exposure, respectively, during three cycles. Undoped NiO exhibits a complex behavior, with a fast-initial resistance drop (resulting in a n-type response) followed by an increase after some seconds (resulting in a p-type response). These results suggest the presence of two competitive mechanisms with opposite influence on the sample sensitivity. On the other hand, Sn doped NiO exhibit some stability contrary to undoped NiO after three cycles, showing a continuous resistance increase under ethanol exposure. Considering that NiO is a p-type semiconductor, different oxygen species should be adsorbed at the surface under air

exposure, thereby leading to free electron capture and increase of the conductivity. This commonly reported sensing mechanism [40], [41] is based on the formation of a hole accumulation layer due to oxygen adsorption. However, when ethanol is injected the adsorbed oxygen could react with the gas which results in a decrease of the hole concentration and the increase in the resistance of the sample. The sensitivity of the sample Ni:SnO_2-(9:1) is nearly the same as that from reference NiO after 3 cycles and demonstrates some stability contrary to NiO. In this case, the Sn doped NiO shows porous islands and grid-patterning at the surface involving a high-surface-area to volume ratio, which should increase the gas reactivity. However, the observed response for the Sn doped samples could be explained attending to the lower hole injection and hole accumulation layer during oxygen adsorption in this sample. One possible reason for this similar response in the Sn doped sample could be attributed to the high adsorbed oxygen species and mostly hydroxyl groups observed before air exposure, as demonstrated by XPS, which hindered the adsorption of new oxygen species and the reaction under ethanol exposure. Actually, a worse response has been observed for the sample Ni:Sn-(9:1), not shown here, probably due to hydroxyl poisoning, as well as increased Sn^{2+} at the surface. The presence of mixed oxidation states of Sn and the higher concentration of microwires in the Sn doped samples can also alter the chemical reactions at the surface and therefore the sensing mechanisms. Usually, gas sensing properties are measured at different operating temperature ranging from 50 ^{o}C to 400 ^{o}C. [42]. In the present work, we have demonstrated a good response for NiO and Ni:SnO_2-(9:1) working at 28 ^{o}C, however, more efforts are necessary in order to understand the influence of mixed oxidation states of Sn and related surface properties not only in the chemical reactions and therefore, the gas sensing properties, but also in some other surface-mediated processes.

The advent of future NiO-based devices requires facing challenging aspects related to the synthesis processes and the achievement of a deeper understanding of the fundamental properties of this p-type material, hence the results described in this work can pave the way to the upgrade of NiO-based applications in diverse fields of research.

4. Conclusions

The presence of Sn with mixed oxidation states during the growth process at 1400 °C under a continuous argon flow has revealed to govern the formation of complex self-assembled grid-pattern structures and microwires at the surface of the Sn doped NiO. By selecting appropriate Sn-based precursor, either SnO_2 or metallic Sn, and its initial concentration, not only the morphological, but also the structural, electrical and optical properties of the singular Sn doped NiO surfaces can be tailored. Oxidation and cationic diffusion controlled mechanisms occurred during the thermal treatments at high temperature should be considered in the growth of the self-assembled surface networks, in which a non-homogeneous presence of mixed Sn^{2+} and Sn^{4+} at the surface and the related variable Ni^{3+}/Ni^{2+} ratio also play key roles. Relevant differences in the Raman spectra and the CL signal have been analysed as a function of selected precursor. The wide CL spectra from Sn doped NiO extend from the near-IR to the UV region, and exhibit a dominant orange emission related to the presence of Ni vacancies. By selective Sn doping, high luminescence can be promoted in the visible range, hence involving promising novel functionality for NiO in optical devices. Higher p-type character is also achieved by Sn doping. Moreover, the enhanced presence of adsorbed oxygen and hydroxyl species at the Sn doped NiO

surfaces has been demonstrated by XPS, which should play a fundamental role in applications such as catalysis or gas sensing, among others.

FIGURES

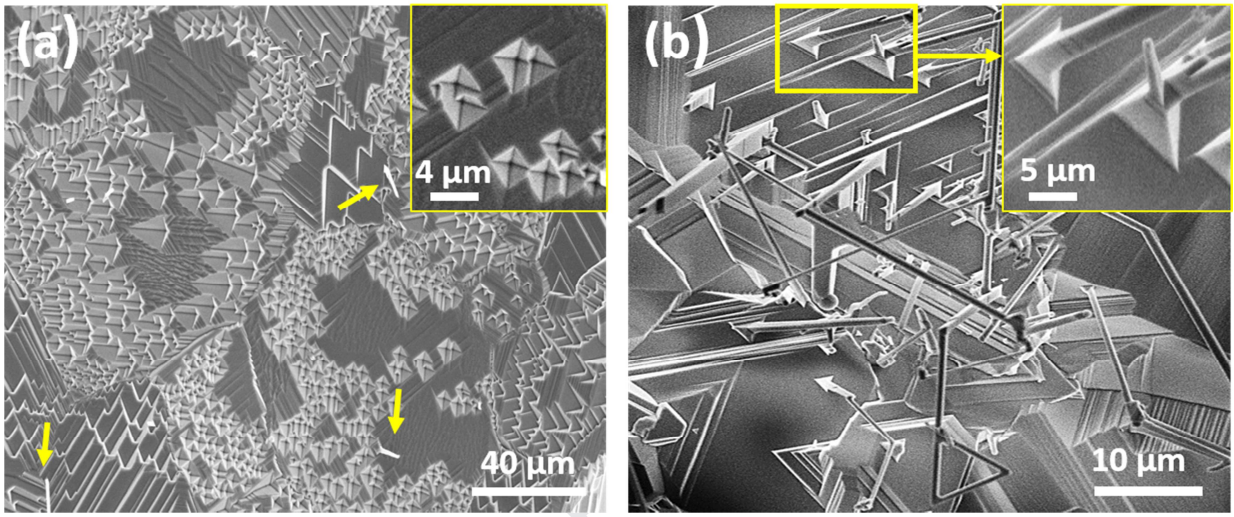

Fig. 1 (a) SEM image from the surface of the reference NiO sample showing microwires, marked with arrows, and a high concentration of pyramidal microcavities. The inset shows a detailed image of some microcavities. (b) Region showing microwires which grow from a triangular terraced base (shown in the inset).

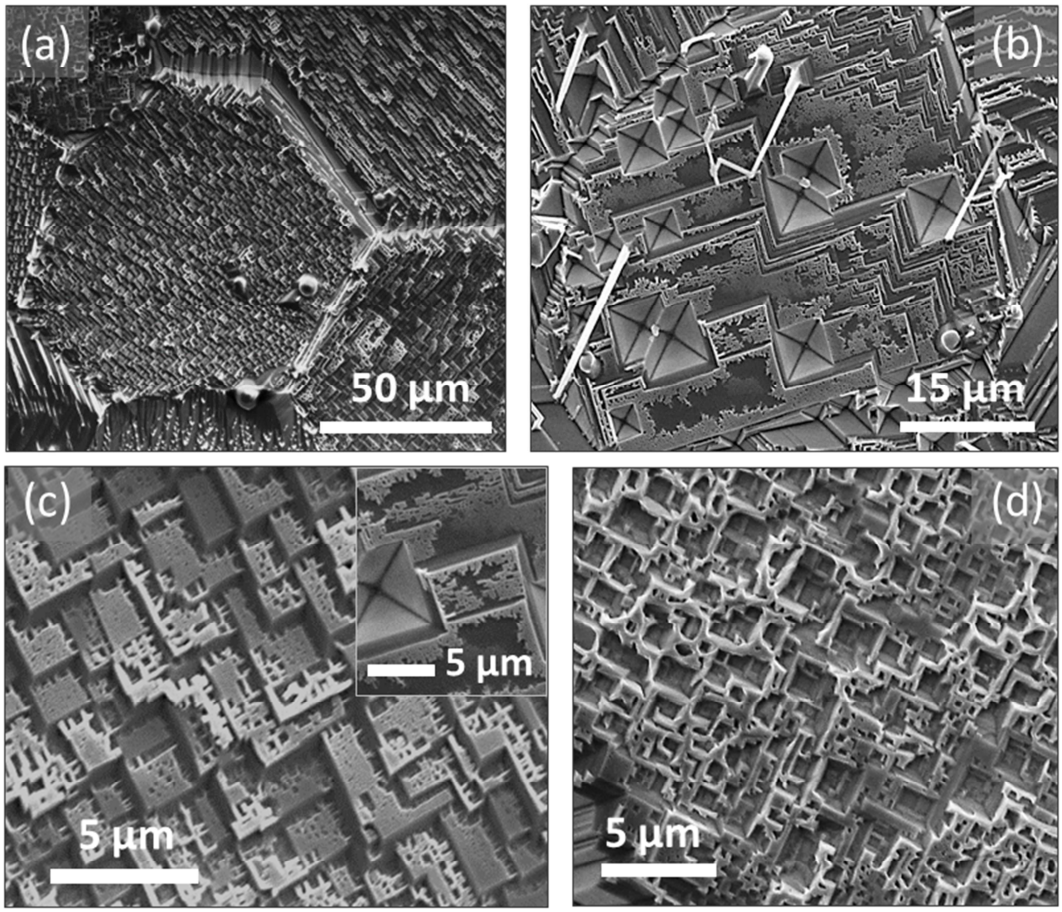

Fig. 2 (a) SEM image from the sample Ni:SnO_2-(9:1) showing micrograins with textured surfaces. (b) Detailed SEM image from the sample Ni:SnO_2-(9:1) (10 hours) where geometrical patterns and microwires can be observed at the surface. (c) SEM image from the sample Ni:SnO_2-(9:1) (10 hours) with nanoporous islands and branched nanostructures forming 2D-networks. (d) SEM image from the sample Ni:SnO_2-(9:1)-b (15 hours) with grid-micropatterning and 3D-network.

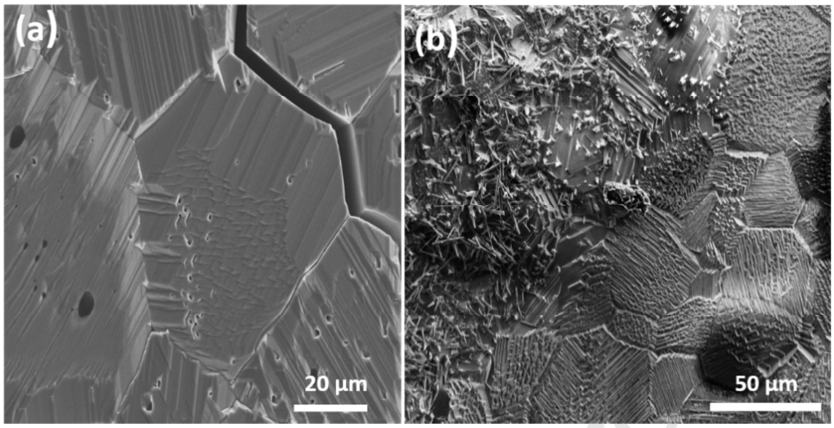

Fig. 3 (a) SEM images from the surface of the sample Ni:SnO_2-(1:1), where the textured surfaces are inhibited. (b) SEM image from the surface of the sample Ni:Sn-(9:1), showing micrograins with a large amount of elongated structures (left side of the image) and terraced appearance (right side of the image).

Journal Pre-proof

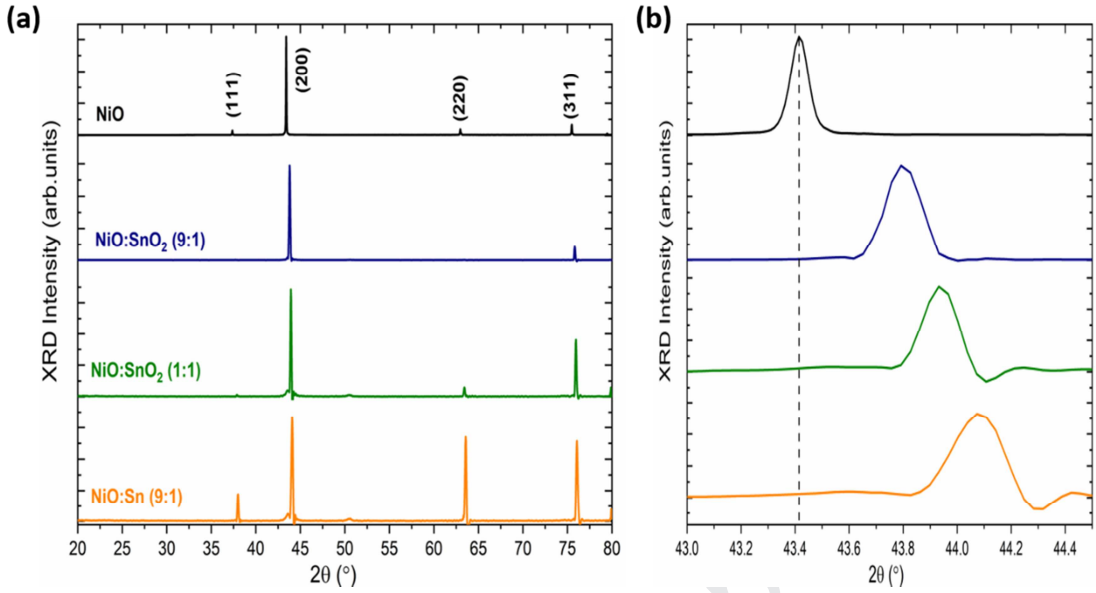

Fig. 4 (a) XRD patterns from the samples, NiO, Ni:SnO_2-(9:1), Ni:SnO_2-(1:1) and Ni:Sn-(9:1) showing rock-salt structure in all the cases (b) Detailed region of the (200) diffraction peak, showing a shift to higher angles in the samples with Sn or SnO_2 incorporation.

Journal Pre-proof

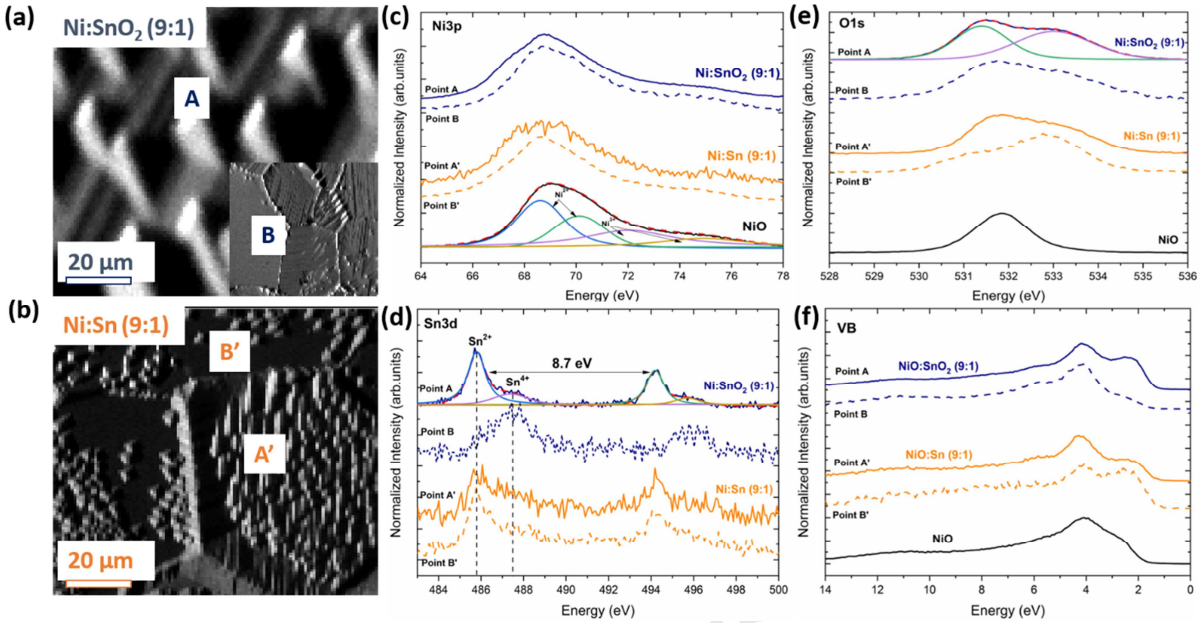

Fig. 5 XPS images acquired with the Ni-3p signal from the surface of the samples (a) Ni:SnO_2-(9:1) and (b) Ni:Sn-(9:1) where different points A, B, A' and B' from analyzed regions are marked. XPS spectra from (c) Ni-3p, (d) Sn-3d, (e) O-1s core levels and (f) valence band region acquired at the points A and B in (a) and A' and B' in (b).

Journal Pre-proof

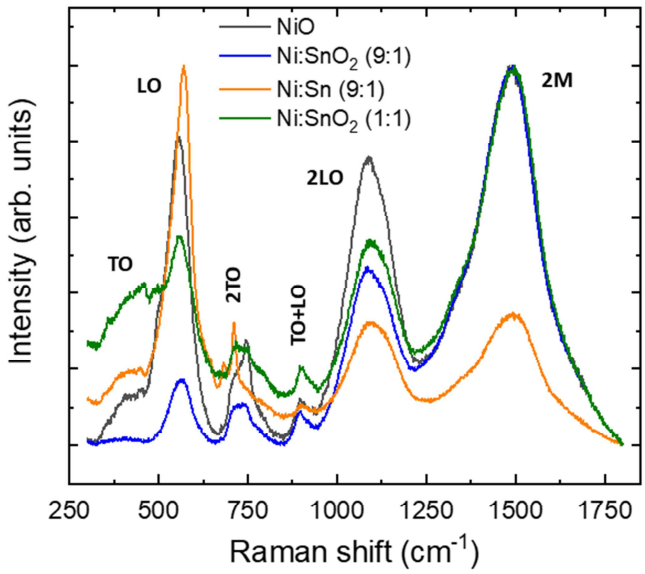

Fig. 6 Normalized Raman spectra from the samples Ni:SnO_2-(9:1), Ni:SnO_2-(1:1), Ni:Sn-(9:1) and the reference NiO sample.

Journal

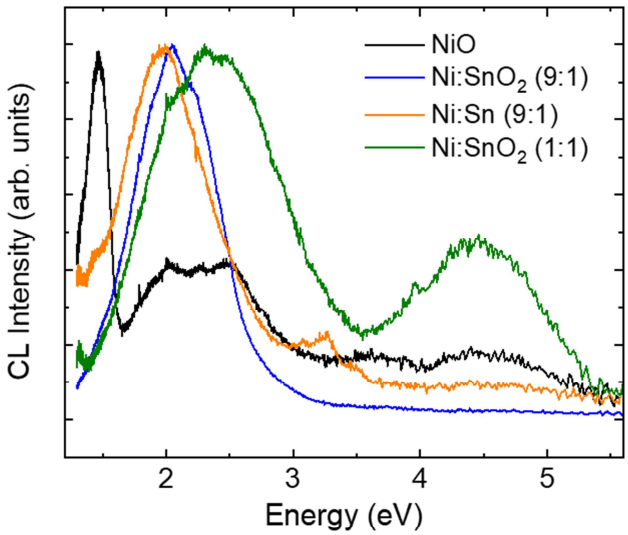

Fig. 7 Normalized CL spectra from the samples Ni:SnO_2-(9:1), Ni:SnO_2-(1:1), Ni:Sn-(9:1) and the reference NiO sample, showing an increase in the relative intensity of the emission of VIS region with Sn or SnO_2 incorporation.

Journal Pre-proof

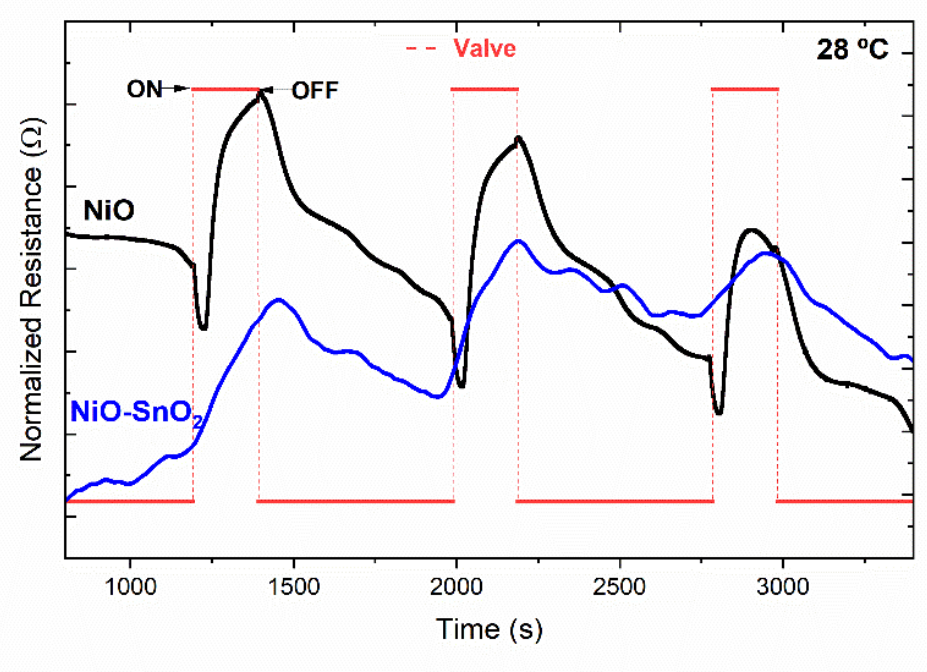

Fig. 8. Normalized resistance from the sample Ni:SnO_2-(9:1) and the reference NiO sample showing the ethanol sensing response at 28 ºC during three cycles.

TABLES

Table 1: List of samples analyzed as a function of the precursors, their selected weight ratio and the corresponding thermal treatment.

Journal Pre

Precursors	Weight ratio	Thermal treatment	Sample
Ni	-	1400 °C (10 h)	NiO
Ni:SnO_2	(9:1)	1400 °C (10 h)	Ni:SnO_2-(9:1)
Ni:SnO_2	(9:1)	1400 °C (15 h)	Ni:SnO_2-(9:1)-b
Ni:Sn	(9:1)	1400 °C (10 h)	Ni:Sn-(9:1)
Ni:SnO_2	(1:1)	1400 °C (10 h)	Ni: SnO_2-(1:1)
Ni: SnO_2	(1:3)	1400 °C (10 h)	Ni: SnO_2-(1:3)

Supporting Information

Thermal treatments under controlled Ar flow, were carried out in a furnace as shown in **Fig. S1**.

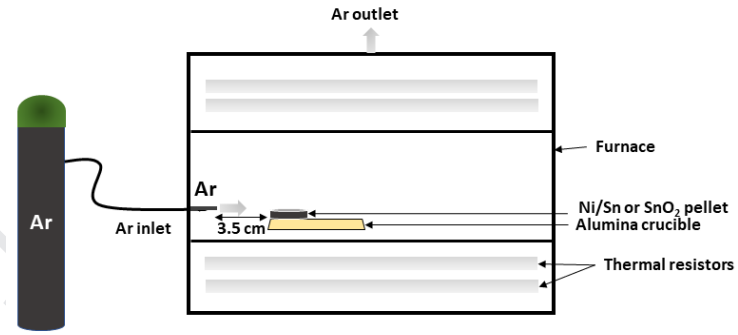

Fig. S1. Scheme of the furnace where thermal treatments were carried out.

Precursor powders were mixed and milled in a centrifugal mill during 5 hours, with different weight ratios. After 5 hours of milling, the mixed precursor powders were pressed into pellets (diameter of 5 mm and thickness between 1-1.5 mm) and placed in a furnace connected to a Argon source. Thermal treatments were carried out at different temperatures, keeping Ar flow in 1.6 l/min and the 3.5 cm distance between the pellet and the Ar inlet, for all the cases. The presence of a continuous and controlled Ar flow, enhances supersaturation conditions, playing a

key role in the formation of the characteristic surface patterns. In addition, **Fig. S2** shows SEM images of NiO, Ni:SnO_2-(9-1) and Ni:Sn-(9:1) treated at 1400 ºC without Ar flow, showing that in those conditions, the formation of textured surfaces, is inhibited.

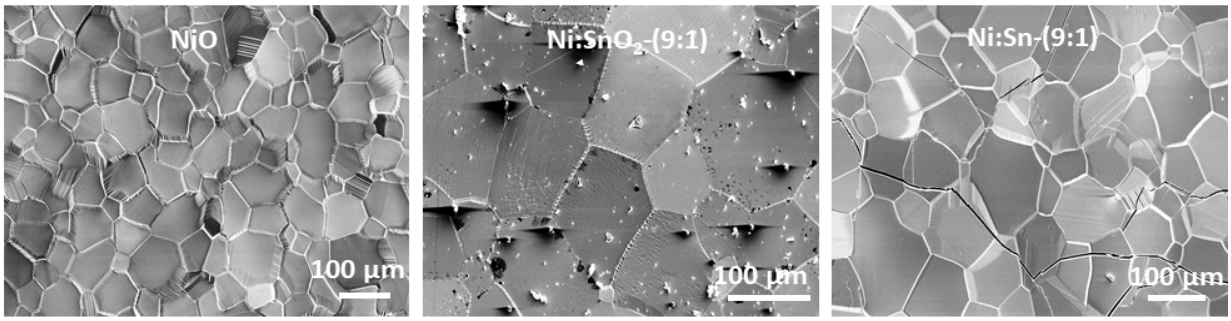

Fig. S2. SEM images from the samples NiO, Ni:SnO_2-(9:1) and Ni:Sn-(9:1) treated without Ar flow, showing a smooth appearance.

In the case of Ni:SnO_2-(1:3) sample, the growth of microwires and geometrical patterns at the surface is completely inhibited. Micrograins with lower dimensions are formed at the surface of the pellet as shown in **Fig. S3 (a)**. The presence of tin has been confirmed by EDS. Either Ni or Sn-rich regions can be observed at the non-homogeneous surface of the pellet, as shown in the compositional EDS image included in the inset of **Fig. S3(a)**. **Fig. S3(b)** shows the diffraction patterns of Ni:SnO_2-(1:3) sample. Weak peaks from SnO_2 start to appear for this sample, although their intensity is very low considering the high amount of SnO_2 used in the precursors.

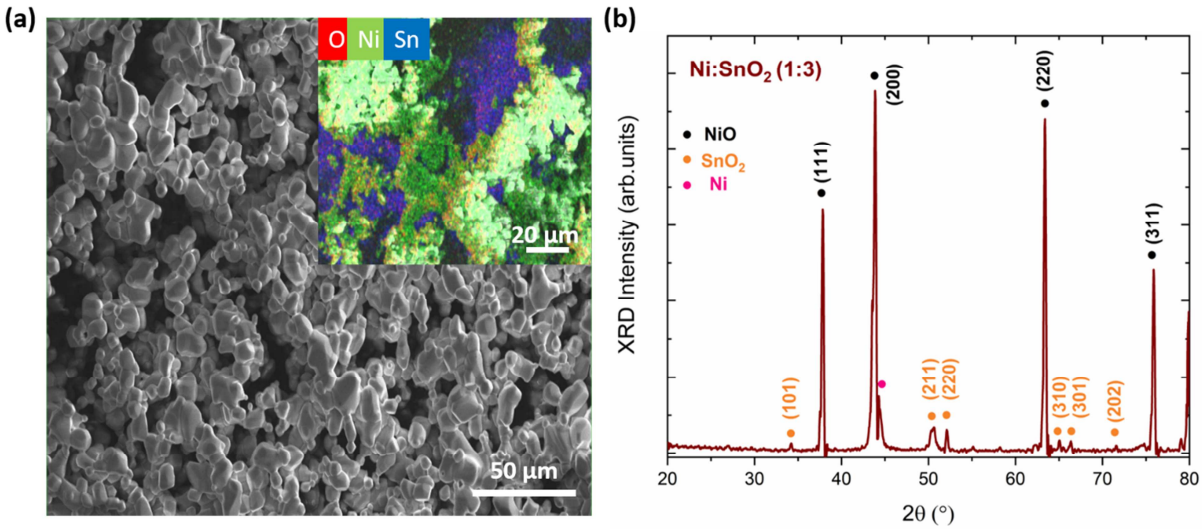

Fig. S3 (a) SEM image and EDS compositional image obtained with the oxygen, tin and nickel signal acquired on the surface of the sample Ni: SnO_2-(1:3). (b) XRD pattern from Ni: SnO_2 (1:3) showing peaks from SnO_2 and NiO, as well as from Ni.

XRD patterns from Ni:SnO_2-(9:1)-b sample is shown in **Fig. S4(a)**. All the peaks can be indexed according to NiO with rock-salt cubic structure, without peaks from the precursors, other oxides or ternary compounds. The intensity of the NiO (200) peak increases for this sample as compared to the sample Ni:SnO_2-(9-1) annealed during 10 hours, which could be related with the initiation of the vertical growth and 3D-grid microstructures for this sample. In order to understand the reason why Sn is not detected at the surface by EDS, cross-sectional EDS compositional images have been acquired, as shown in **Fig. S4(b)**. Compositional mapping and EDS spectra confirm that the amount of Sn increases in the inner region of the pellet, while the surface is mainly formed by Ni and O, probably due to variable cationic diffusion during crystal growth and possible SnO_2 segregation to the core of the pellet.

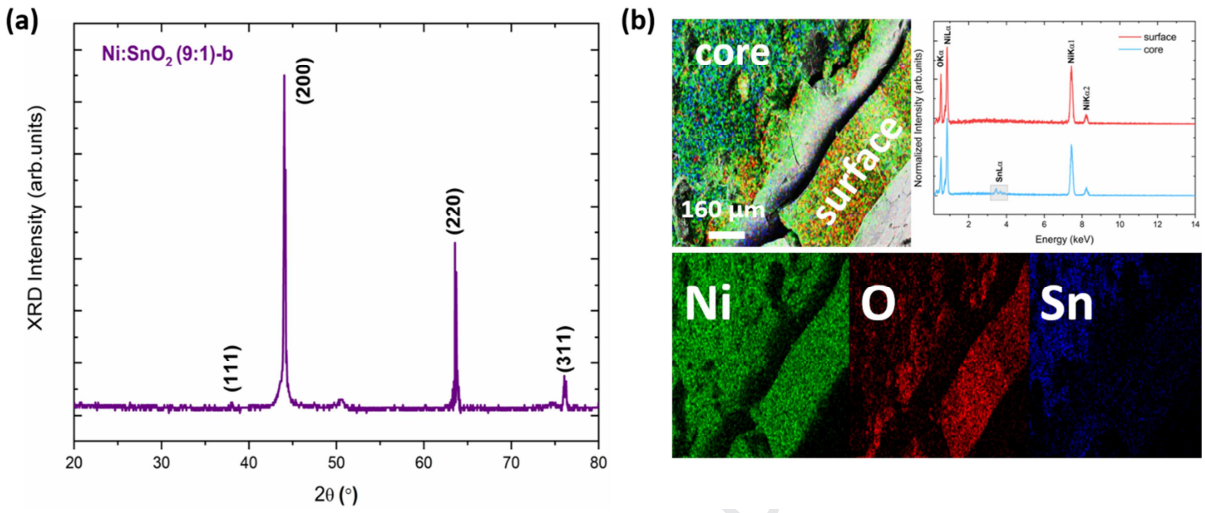

Fig. S4 (a) XRD patterns and (b) EDS image of a cross sectional view of a sample Ni: SnO_2 (9:1)-b, showing compositional images obtained with oxygen, tin and nickel signal. EDS spectra acquired at the surface and at the core of the pellet are also included.

The chromaticity coordinates from the measured CL spectra of the samples, according to the *Comission Internationale l'Eclairage* (CIE 1931) standard, have been plotted in the chromaticity diagram as shown in **Fig S5**. The spots represent the color from the CL spectra, showing that the luminescent signal of NiO can be tailored by selecting appropriate Sn precursor and concentration.

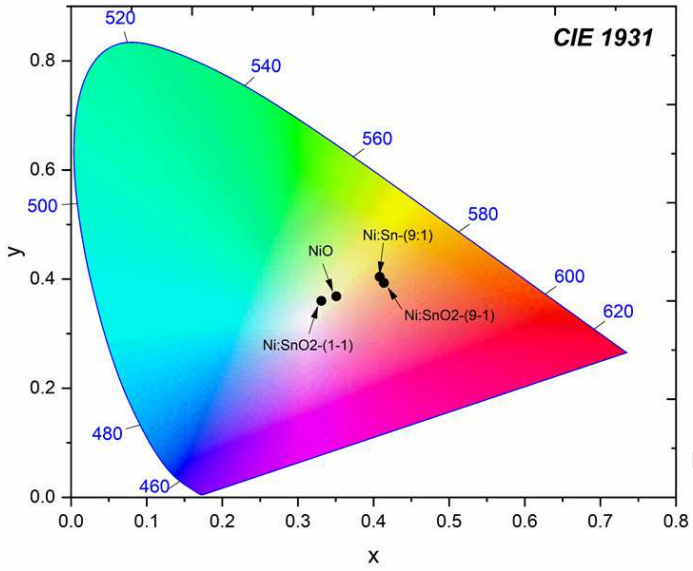

Fig. S5. *CIE 1931 chromaticity coordinates of the CL spectra showed in Fig.7*

The sensing system employed in this work is shown in **Fig. S6**. The system is equipped with seven valves in order to control the ethanol and N_2 flow. The sensing cycles are divided in three different steps:

1. An air purged current is introduced in the system for 1200 seconds. During this process the oxygen species are adsorbed at the surface of the NiO pellets.

2. A mix flow of ethanol and air is introduced in the chamber for 200 seconds, where the oxygen species adsorbed in the previous step react with ethanol following this reaction:

   $C_2H_5OH + O_{ads}^-/O_2^- \rightarrow CO_2 + H_2O + e^-$

3. During the recovery process, another air purged current is introduced in the system for 600 seconds, then another flow of ethanol and air is introduced in the chamber.

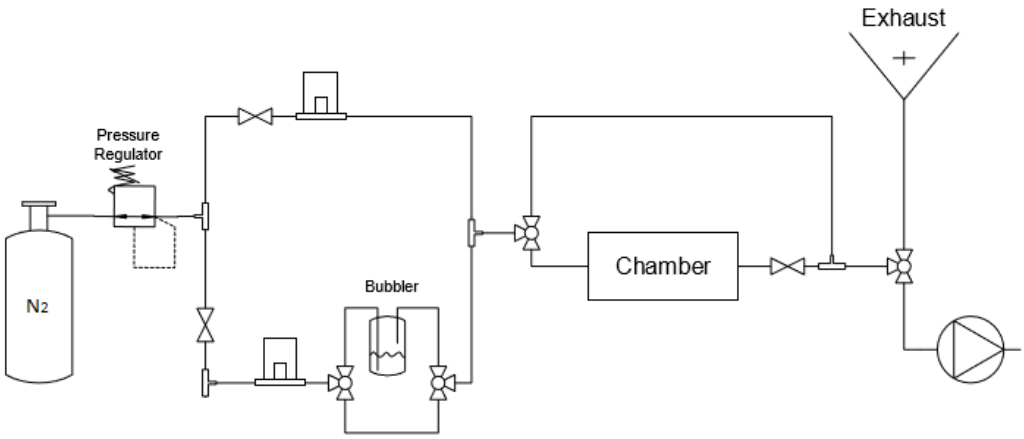

Fig. S6. Scheme of the gas sensing experimental set-up

Corresponding Author

*Phone: (+34)91394496. E-mail: m.taeno@ucm.es

Author Contributions

The manuscript was written through contributions of all authors. All authors have given approval to the final version of the manuscript. All the authors contributed equally.

Acknowledgements

Authors thank the ESCA-microscopy staff at the Elettra Synchrotron for their help during XPS measurements.

Funding Sources

The work was supported by MINECO/FEDER/M-ERA.Net Cofund projects: MAT 2015-65274-R, RTI2018-097195-B-I00 and PCIN-2017-106.

Graphical Abstract

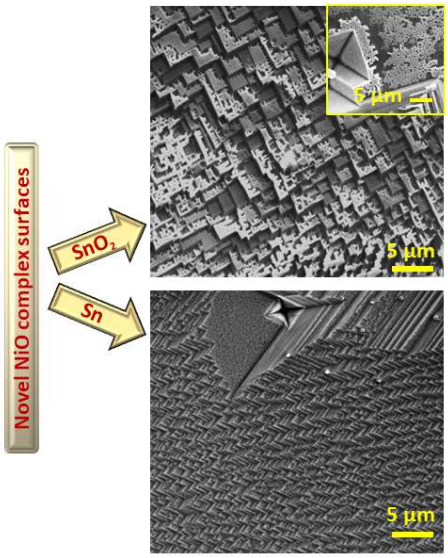

References

[1] T. Moriyama, K. Oda, T. Ohkochi, M. Kimata, T. Ono, Spin torque control of antiferromagnetic moments in NiO, Scientific Reports 8(1) (2018) 14167.

[2] G. Cai, X. Wang, M. Cui, P. Darmawan, J. Wang, A.L.-S. Eh, P.S. Lee, Electrochromo-supercapacitor based on direct growth of NiO nanoparticles, Nano Energy 12 (2015) 258-267.
[3] W. Chen, Y. Wu, J. Fan, A.B. Djurišić, F. Liu, H.W. Tam, A. Ng, C. Surya, W.K. Chan, D. Wang, Z.-B. He, Understanding the Doping Effect on NiO: Toward High-Performance Inverted Perovskite Solar Cells, Advanced Energy Materials 8(19) (2018) 1703519.
[4] V. Sandana, D. Rogers, F. H. Teherani, P. Bove, N. Ben sedrine, M. Correia, T. Monteiro, R. McClintock, M. Razeghi, Structural, Optical, Electrical and Morphological Study of Transparent p-NiO/n-ZnO Heterojunctions Grown by PLD, Proc SPIE 9364 (2015) 93641O-1.
[5] X. Xu, L. Li, J. Huang, H. Jin, X. Fang, W. Liu, N. Zhang, H. Wang, X. Wang, Engineering Ni3+ Cations in NiO Lattice at the Atomic Level by Li+ Doping: The Roles of Ni3+ and Oxygen Species for CO Oxidation, ACS Catalysis 8(9) (2018) 8033-8045.
[6] E. Heracleous, A.A. Lemonidou, Ni-Nb-O mixed oxides as highly active and selective catalysts for ethene production via ethane oxidative dehydrogenation. Part II: Mechanistic aspects and kinetic modeling, J. Catal. 237(1) (2006) 175-189.
[7] B.-Y. Kim, J.-W. Yoon, J.K. Kim, Y.C. Kang, J.-H. Lee, Dual Role of Multiroom-Structured Sn-Doped NiO Microspheres for Ultrasensitive and Highly Selective Detection of Xylene, ACS Applied Materials & Interfaces 10(19) (2018) 16605-16612.
[8] H. Gao, D. Wei, P. Lin, C. Liu, P. Sun, K. Shimanoe, N. Yamazoe, G. Lu, The design of excellent xylene gas sensor using Sn-doped NiO hierarchical nanostructure, Sensors and Actuators B: Chemical 253 (2017) 1152-1162.
[9] Z. Wang, H. Zhou, D. Han, F. Gu, Electron compensation in p-type 3DOM NiO by Sn doping for enhanced formaldehyde sensing performance, Journal of Materials Chemistry C 5(13) (2017) 3254-3263.
[10] L.S. Nair, D. Chandran, V.M. Anandakumar, K. Rajendra Babu, Structure and room-temperature ferromagnetism evolution of Sn and Mn-doped NiO synthesized by a sol-gel process, Ceramics International 43(14) (2017) 11090-11096.
[11] Z. Liliental-Weber, J. Jasinski, M. Benamara, I. Grzegory, S. Porowski, D.J.H. Lampert, C.J. Eiting, R.D. Dupuis, Influence of Dopants on Defect Formation in GaN, Physica Status Solidi (b) 228(2) (2001) 345-352.
[12] J. Bartolomé, D. Maestre, M. Amati, A. Cremades, J. Piqueras, Indium Zinc Oxide Pyramids with Pinholes and Nanopipes, The Journal of Physical Chemistry C 115(16) (2011) 8354-8360.
[13] A.A. Dakhel, Investigations on Sn-doped Ni oxide thin films and their use as optical sensor devices, Journal of Non-Crystalline Solids 358(2) (2012) 285-289.
[14] D. Varshney, S. Dwivedi, Synthesis, structural, Raman spectroscopic and paramagnetic properties of Sn doped NiO nanoparticles, Superlattices and Microstructures 86 (2015) 430-437.
[15] N. Halem, M. Abrudeanu, G. Petot-Ervas, Al effect in transport properties of nickel oxide and its relevance to the oxidation of nickel, Materials Science and Engineering: B 176(13) (2011) 1002-1009.
[16] Y. Unutulmazsoy, R. Merkle, D. Fischer, J. Mannhart, J. Maier, The oxidation kinetics of thin nickel films between 250 and 500 °C, Physical Chemistry Chemical Physics 19(13) (2017) 9045-9052.
[17] X. Ning, Z. Wang, Z. Zhang, Fermi Level shifting, Charge Transfer and Induced Magnetic Coupling at La0.7Ca0.3MnO3/LaNiO3 Interface, Scientific Reports 5(1) (2015) 8460.
[18] L. Qiao, X. Bi, Direct observation of Ni3+and Ni2+in correlated LaNiO3−δfilms, EPL (Europhysics Letters) 93(5) (2011) 57002.

[19] F.d. Prado, A. Cremades, D. Maestre, J. Ramírez-Castellanos, J.M. González-Calbet, J. Piqueras, Controlled synthesis of lithium doped tin dioxide nanoparticles by a polymeric precursor method and analysis of the resulting defect structure, Journal of Materials Chemistry A 6(15) (2018) 6299-6308.
[20] E.L. Ratcliff, J. Meyer, K.X. Steirer, A. Garcia, J.J. Berry, D.S. Ginley, D.C. Olson, A. Kahn, N.R. Armstrong, Evidence for near-Surface NiOOH Species in Solution-Processed NiOx Selective Interlayer Materials: Impact on Energetics and the Performance of Polymer Bulk Heterojunction Photovoltaics, Chemistry of Materials 23(22) (2011) 4988-5000.
[21] J.-M. Themlin, M. Chtaïb, L. Henrard, P. Lambin, J. Darville, J.-M. Gilles, Characterization of tin oxides by x-ray-photoemission spectroscopy, Physical Review B 46(4) (1992) 2460-2466.
[22] C. Wagner, Beitrag zur Theorie des Anlaufvorgangs, Zeitschrift für Physikalische Chemie, B21 (1933), 25.
[23] W.H. Blades, P. Reinke, From Alloy to Oxide: Capturing the Early Stages of Oxidation on Ni–Cr(100) Alloys, ACS Applied Materials & Interfaces 10(49) (2018) 43219-43229.
[24] M.R.J. Scherer, U. Steiner, Efficient Electrochromic Devices Made from 3D Nanotubular Gyroid Networks, Nano Letters 13(7) (2013) 3005-3010.
[25] A. Atkinson, Transport Processes During the Growth of Oxide Films at Elevated Temperature, Reviews of Modern Physics - REV MOD PHYS 57 (1985) 437-470.
[26] I. Gallino, R. Busch, H.C. Yim, L. Jastrow, U. Köster, High temperature oxidation of the refractory alloy glass Nb35Ni60Sn5, Journal of Alloys and Compounds 434-435 (2007) 225-228.
[27] I. McCue, E. Benn, B. Gaskey, J. Erlebacher, Dealloying and Dealloyed Materials, Annual Review of Materials Research 46(1) (2016) 263-286.
[28] M. Altomare, N.T. Nguyen, P. Schmuki, Templated dewetting: designing entirely self-organized platforms for photocatalysis, Chemical Science 7(12) (2016) 6865-6886.
[29] N. Mironova-Ulmane, A. Kuzmin, I. Sildos, M. Pärs, Polarisation dependent Raman study of single-crystal nickel oxide, Central European Journal of Physics 9(4) (2011) 1096-1099.
[30] M.M. Lacerda, F. Kargar, E. Aytan, R. Samnakay, B. Debnath, J.X. Li, A. Khitun, R.K. Lake, J. Shi, A.A. Balandin, Variable-temperature inelastic light scattering spectroscopy of nickel oxide: Disentangling phonons and magnons, Appl. Phys. Lett. 110 (2017) 202406.
[31] A.C. Gandhi, C.-Y. Huang, C.C. Yang, T.S. Chan, C.-L. Cheng, Y.-R. Ma, S.Y. Wu, Growth mechanism and magnon excitation in NiO nanowalls, Nanoscale Res Lett 6(1) (2011) 485-485.
[32] A.C. Gandhi, S.Y. Wu, Strong Deep-Level-Emission Photoluminescence in NiO Nanoparticles, Nanomaterials (Basel) 7(8) (2017) 231.
[33] S. I. Córdoba-Torresi, A. H. L. Gaff, S. Joiret, Electrochromic Behavior of Nickel Oxide Electrodes, Journal of The Electrochemical Society - J ELECTROCHEM SOC 138 (1991) 1554.
[34] E. Aytan, B. Debnath, F. Kargar, Y. Barlas, M.M. Lacerda, J.X. Li, R.K. Lake, J. Shi, A.A. Balandin, Spin-phonon coupling in antiferromagnetic nickel oxide, Applied Physics Letters 111(25) (2017) 252402.
[35] A. Kuzmin, N. Mironova-Ulmane, S. Ronchin, Origin of visible photoluminescence in NiO and NicMg1-cO single-crystals, Proc SPIE 5122 (2003) 61-67.
[36] C. Díaz-Guerra, A. Remón, J.A. García, J. Piqueras, Cathodoluminescence and Photoluminescence Spectroscopy of NiO, Physica Status Solidi (a) 163(2) (1997) 497-503.
[37] Z. Zhang, Y. Zhao, M. Zhu, NiO films consisting of vertically aligned cone-shaped NiO rods, Applied Physics Letters 88(3) (2006) 033101.

[38] D. Maestre, A. Cremades, J. Piqueras, Cathodoluminescence of defects in sintered tin oxide, Journal of Applied Physics 95(6) (2004) 3027-3030.
[39] W. Mackrodt, S. Salustro, B. Civalleri, R. Dovesi, Low energy excitations in NiO based on a direct Δ-SCF approach, Journal of Physics: Condensed Matter 30 (2018) 495901.
[40] C. Zhao, J. Fu, Z. Zhang, E. Xie, Enhanced ethanol sensing performance of porous ultrathin NiO nanosheets with neck-connected networks, RSC Advances 3 (2013) 4018-4023
[41] H. J. Kim, H. M. Jeong, T. H. Kim, J. H. Chung, Y. C. Kang, J. H. Lee, Enhanced Ethanol Sensing Characteristics of In_2O_3-Decorated NiO hollow nanostructures via Modulation of Hole Accumulation Layers, ACS Appl. Mater. Interfaces 6 (2014) 18197-18204
[42] G. Zhang, X. Han, W. Bian, J. Zhan, X. Ma. Facile synthesis and high formaldehyde-sensing performance of NiO-SnO_2 hybrid nanospheres, RSC Advances 6 (2016) 3919-3926

Journal Pre-proof

Journal Pre-proof

HIGHLIGHTS

"**Fabrication and Study of Self-assembled NiO Surface Networks Assisted by Sn Doping"**

M. Taeño*, D. Maestre, and A. Cremades

- Fabrication of singular grid-pattern NiO surfaces by self-assembled mechanisms using thermal treatments.
- Enhanced luminescence and variable Raman signal on the Sn doped NiO samples.
- Study of selective Sn doping with variable Sn^{2+}/Sn^{4+} ratio and achievement of high p-type character

Journal Pre-proof

Journal Pre-proof

Declaration of interests

☒ The authors declare that they have no known competing financial interests or personal relationships that could have appeared to influence the work reported in this paper.

☐The authors declare the following financial interests/personal relationships which may be considered as potential competing interests:

Journal Pre-proof